

## Analysis and modeling of thermal-blooming compensation

Jonathan F. Schonfeld  
Lincoln Laboratory, Massachusetts Institute of Technology  
P. O. Box 73, Lexington, Massachusetts 02173

ABSTRACT

This paper surveys work of the last several years at Lincoln Laboratory in analysis and computer modeling of adaptive optics hardware, especially in the context of compensation for thermal blooming. We discuss an analytical theory of thermal blooming phase-compensation instability (PCI) incorporating the actuator geometry of real deformable mirrors and wavefront sensors; we also discuss novel algorithms for computer simulation of adaptive optics hardware. Our analytical formalism makes possible a quantitative analysis of the effects of the adaptive-optics control system on PCI, and also leads to a universality theorem for PCI growth rates under certain control-system assumptions. It also leads to the recognition that wind has a stronger effect on PCI growth rates than previously thought. Simulation algorithms discussed here include models of a Hartmann wavefront sensor, multidither adaptive optics, and a null-seeking servo. Analysis and algorithms are illustrated with output from MOLLY, a computer simulation of time-dependent adaptively-compensated laser propagation through turbulence and thermal blooming, optimized for the Cray-2 supercomputer. Of particular note is a comparison between MOLLY output and data from a laboratory study of phase-compensation instability.

I. INTRODUCTION

This paper surveys work of the last several years at Lincoln Laboratory in analysis and computer modeling of adaptive optics hardware, especially in the context of compensation for thermal blooming, the spreading of a laser beam that results when the absorption of some of its energy perturbs refractivity in the atmosphere. Detailed analysis and simulation of adaptive optics hardware are obviously important for engineering. As we shall see, they also provide valuable insight into fundamental processes such as thermal blooming phase-compensation instability.

The work described here was performed in the course of developing, applying and interpreting a computer simulation, MOLLY, of time-dependent adaptively-compensated laser propagation through turbulence and thermal blooming. (Simulation output will be used later to illustrate our analysis and algorithms.) MOLLY was initially developed in 1986-87 in response to observations of dramatic structure on small spatial scales in steady-state simulations of compensated strong thermal blooming, in order to establish that such behavior (now understood as phase-compensation instability and turbulence/thermal-blooming interaction) was not a numerical artifact. MOLLY has since been used to explore the behavior of adaptive optics systems under many environmental and instrumental conditions, for a variety of lasers. Of particular note is the use of MOLLY to model an ongoing experimental study of compensated thermal blooming at Lincoln Laboratory.

The emphasis in this paper will be on advances in analytical and modeling techniques. We shall illustrate these techniques with applications both to simulation and to non-computational theory.

This paper is organized as follows: In Section II, we introduce some basic concepts from adaptive optics. In Section III, we discuss analysis of the interplay between adaptive optics design and thermal blooming phase-compensation instability. In Section IV, we describe novel algorithms for computational modeling of adaptive optics hardware. In Section V, we illustrate these developments with output from simulations of compensated propagation through the atmosphere and in the laboratory. The paper is summarized in Section VI.

II. BASIC CONCEPTS IN ADAPTIVE OPTICS

The basic components of a conventional phase-conjugate adaptive optics system (Figure 2.1.) are wavefront sensor, deformable mirror (supplemented by a tilt mirror) and control system. In addition, a beacon source is needed to provide incoming radiation that contains information about phase aberrations present between the outgoing laser source and the target. An aperture-sharing element (ASE) isolates beacon detecting equipment against light from the outgoing source.

The wavefront sensor measures incoming phase, one measurement per node on a two-dimensional Cartesian grid. The deformable mirror deforms in accordance with voltages applied to actuators at the nodes of another two-dimensional grid, aligned with the wavefront sensor. The control system transforms phase measurements to actuator voltages. Ideally, the

voltages are such that the phase of the outgoing beam, after reflection from the deformable mirror, is nearly conjugate to the phase of the incoming beam, up to wavelength scaling.

An example of a wavefront sensor, the Hartmann sensor, is shown schematically in Figure 2.2. The incoming beam is intercepted by an array of lenslets that bring subapertures of the beam to focus. Mean subaperture phase gradients are inferred from the positions of the focal-spot centroids. Phase measurements are reconstructed from these gradient measurements.

Deformable mirror figure  $f(\mathbf{x})$  is related to actuator voltages  $v_n$  via the influence function  $f$ , according to

$$\phi(\mathbf{x}) = \sum_n v_n f(\mathbf{x} - n\mathbf{d}), \quad (2.1)$$

where  $\mathbf{x}$  is position in the deformable mirror plane,  $\mathbf{n}$  is a two-dimensional integer vector, and  $d$  is actuator spacing.

We distinguish two broad classes of control systems: deformable mirror in beacon path ("in-path") and out of beacon path ("out-of-path") (Figure 2.3). When deformable mirror is in-path, the beacon reflects off the deformable mirror before entering the wavefront sensor. Thus, the wavefront sensor measures the difference between the phase that the beacon develops in the course of propagation and the correction phase applied to the outgoing beam. The system treats this difference as an error signal, either adding it (after suitable scaling) to deformable mirror voltage, or driving it to zero with a ("null-seeking") servo. When deformable mirror is out-of-path, the beacon never encounters the deformable mirror, so the wavefront sensor measures only the phase accumulated during propagation. Out-of-path systems are easier to model because there is no direct feedback between the wavefront sensor and deformable mirror. However, systems with deformable mirror in-path are preferred by experimentalists because measurement of error phases places weaker demands on a wavefront sensor's dynamic range than does measurement of uncompensated phases. For this reason, we have worked to incorporate in-path control in our analytical formalisms and simulation algorithms.

For a more detailed discussion of modern adaptive optics technology, see Reference 1.

We distinguish two broad types of adaptive optics model: field-based and phase-based. In a field-based model, phase measurements are derived from the real and imaginary parts of the beacon complex field. In a phase-based model, only the phase of the incoming field is used in deriving phase measurements. Field-based modeling is obviously more realistic. Phase-based models can be simpler to program and computationally more economical because only one real array (phase) is involved. Disadvantages of phase-based modeling include the inability to provide information about a real system's response to beacon intensity structure, and the difficulty of defining incoming phase at all computational grid points without  $2\pi$  ambiguity. When phase-based simulations have been performed with MOLLY, the beacon propagation path has been divided into small steps, so that phase change through any step is small and therefore computable by simple arctangents. Incoming phase has then been defined by accumulating such small stepwise phase changes. The phase-based model originally implemented in MOLLY (now supplanted by field-based models) identified wavefront sensor output with arithmetic averages of incoming phase over square subapertures. The subapertures had side = actuator spacing, and were centered at deformable mirror actuators.

Many workers have modeled the transformation of incoming to outgoing phase or field as simple multiplication by a filter function in the Fourier domain. This idealization is becoming less common in computer simulations, but remains common practice in analysis. All work described in this paper takes full account of the lattice geometry of real adaptive optics.

### III. ADAPTIVE OPTICS DESIGN AND PHASE-COMPENSATION INSTABILITY

Phase-compensation instability (PCI) refers to positive feedback between adaptive-optics hardware and laser-induced atmospheric heating. PCI arises because the correction system focuses the outgoing laser beam into atmospheric hot spots – where atmospheric refractivity is depressed – making them hotter. PCI is important because when absorption is strong or when the outgoing laser is powerful, this feedback can engender rapid growth of dramatic variation in laser amplitudes and phases on small scales transverse to the propagation axis (Figure 3.1). This is incompatible with good adaptive-optics correction when the scale of variation becomes comparable to the separation between deformable-mirror actuators.

Thermal blooming phase-compensation instability is generally analyzed by linearization in small perturbations about propagation with spatially uniform phases and irradiances.<sup>2</sup> The central goal of linearized PCI analysis is an equation for the unstable exponential growth rate,  $\Omega$ , of a perturbation with wavevector  $\mathbf{p}$  in the plane transverse to the propagation axis.

The original linearized analysis of PCI assumed a filter-based adaptive optics model. We have extended this theory to incorporate the discrete actuator pattern of real adaptive optics, with important consequences. We sketch this work here; further details will be published elsewhere.<sup>3</sup>

The formal structure of our analysis is closely related to the earlier filter-oriented theory: When adaptive optics is assumed to be filter-like, the growth-rate equation takes the general form

$$1 = g(\mathbf{p})E(k, \alpha, \mathbf{v}, I, \mathbf{p}, \Omega), \quad (3.1)$$

where  $g$  is the filter function (or "coupling"),  $k$  is optical wavenumber,  $\alpha$  and  $\mathbf{v}$  – functions of propagation distance – are absorptivity and wind,  $I$  is outgoing laser irradiance, and where the functional  $E$  need not be specified here. When a realistic discrete actuator pattern is taken into account, Equation (3.1) is replaced by

$$1 = \sum_{\mathbf{n}} A(d\mathbf{p}_{\mathbf{n}})B(d\mathbf{p}_{\mathbf{n}})E(k, \alpha, \mathbf{v}, I, \mathbf{p}_{\mathbf{n}}, \Omega), \quad (3.2)$$

where  $E$  is the same as in Equation (3.1),  $d$  is actuator spacing,  $\mathbf{n}$  is a two-component integer vector,

$$\mathbf{p}_{\mathbf{n}} \equiv \mathbf{p} - \frac{2\pi\mathbf{n}}{d}, \quad (3.3)$$

where the form factor  $A$  can be derived from the design of the wavefront sensor, and where the form factor  $B$  can be derived from the designs of wavefront sensor, deformable mirror and control system. One can prove that  $B(\mathbf{p})$  is proportional to the influence function's Fourier transform,  $d^2F(d\mathbf{p})$ , for deformable mirror out-of-path, when actuator voltages are proportional to phase measurements (a common convention). For deformable mirror in-path (and infinite bandwidth), one can prove that  $B$  is instead given in terms of  $F$  and  $A$  by

$$B(d\mathbf{p}) = \frac{F(d\mathbf{p})}{\sum_{\mathbf{n}} A(d\mathbf{p}_{\mathbf{n}})F(d\mathbf{p}_{\mathbf{n}})}. \quad (3.4)$$

In many cases of interest, the sum in Equation (3.4) can be expressed in closed form in terms of simple trigonometric functions. Clearly, guesswork in choosing the filter  $g$  has been replaced by well-defined formulas for  $A$  and  $B$  in terms of basic properties of basic hardware.

This formalism is important primarily because it makes practical the quantitative calculation of PCI growth rates for specific realistic adaptive-optics designs. For example, growth rates calculated from Equation (3.2) for the two definitions of  $B$  mentioned above are shown in Figure 3.2. The contrast in this figure suggests that control system design could have a meaningful impact on system performance in the presence of appreciable thermal blooming. This is consistent with simulations to be discussed in Section V.

This formalism also has important general consequences:

- One can prove that growth rates for in-path systems are roughly independent of detailed wavefront sensor and deformable mirror structure. This "universality" is important for numerical simulation of in-path systems: It guarantees that if one must sacrifice simulation realism for reasons of computational economy, one's simulation may nonetheless correctly represent many effects of PCI as long as the adaptive optics model – no matter how unrealistic – incorporates the correct pattern of discrete actuators, and incorporates in-path control. This is consistent with simulations to be discussed in Section V.

- One can also prove that a growth rate's real part is sensitive to the relative orientations of the actuator grid's Cartesian axes, the perturbation wavevector  $\mathbf{p}$ , and the wind  $\mathbf{v}$ , even for uniform wind. Example: When  $\mathbf{p}$  has length  $\pi/d$ , and is parallel both to uniform  $\mathbf{v}$  and to an axis of the actuator grid, then Equation (3.2) can approximately be reduced to the form (3.1), where the coefficient  $g$  for strong wind is half what it is for weak wind. (An intuitive explanation is illustrated in Figure 3.3) This is important because in filter models, by contrast, real parts of growth rates are independent of  $\mathbf{v}$  when wind is uniform. This detracts from the general usefulness of simple filter models.

#### IV. COMPUTATIONAL ALGORITHMS FOR ADAPTIVE OPTICS MODELING

In this section we describe several novel adaptive-optics algorithms developed for our propagation code MOLLY. This code – although portably written in FORTRAN 77 – is optimized for a Cray-2 supercomputer in order to apply that machine's large memory (256 million 64-bit words) to the numerical resolution of thermal-blooming-induced small-scale structure distributed over long propagation paths. In particular, the algorithms discussed below were all designed to exploit vector-processing computer hardware. They were also designed to have operation count for any grid calculation proportional (up to logarithms) to the number of points in the grid (field or actuator).

For readers who are unfamiliar with propagation modeling, here is a brief description of MOLLY's general design: MOLLY idealizes laser transmission as a sequence of instantaneous pulses. (Multiline propagation is realized by assigning distinct wavelengths, energies, absorption and scattering profiles, and initial conditions [irradiance profile, beam quality] to distinct pulses.) Spatial propagation of a pulse is accomplished by dividing the total propagation distance into steps, and within each step approximating laser evolution by a standard<sup>4</sup> three-substep process. In the first and third substeps the laser field advances under the influence of diffraction alone; in the middle substep the laser field advances with no diffraction whatsoever. This approximation is accurate and numerically stable, and also computationally economical because it involves only fast Fourier transforms and simple point-by-point multiplication. Between laser pulses the atmosphere (optical turbulence and laser-induced heating) evolves under the combined influence of wind transport and thermal diffusion. Wind transport and thermal diffusion of laser-induced heating are accomplished by a Fourier filter (supplemented by suitable masking at the edges of computational grids, to inhibit Gibbs oscillation and periodic wraparound). Other transport algorithms could artificially smooth physical small-scale structure. Optical turbulence is defined on grids that overfill the laser apertures, that are transported by the wind in frozen flow, and that are interpolated onto the laser computational grids when needed for propagation.

##### IV.A Hartmann algorithm

We begin by discussing the field-based Hartmann algorithm that presently provides the default wavefront sensor model in MOLLY.

Hartmann modeling is challenging because literally simulating its focusing optics can place heavy demands on numerical resolution. For this reason, we have developed a Hartmann algorithm that refers only to pupil plane data.

This algorithm generates a subaperture gradient measurement (in, say, the  $x$  direction) by evaluating

$$\frac{\int \text{Im} \left( \psi^* \frac{\partial \psi}{\partial x} \right) d^2x}{\int |\psi|^2 d^2x}, \quad (4.1)$$

where  $\psi$  is beacon complex field, and the integrals are restricted to a subaperture in the lenslet pupil plane. This is mathematically equivalent (Parseval's Fourier-transform theorem) to the usual measurement based on the focal centroid. This expression becomes more intuitive when the beacon field is expressed as  $\sqrt{I} \cdot \exp(i\phi)$ , where  $I$  is irradiance and  $\phi$  is phase; in these terms, Expression (4.1) becomes

$$\frac{\int I \frac{\partial \phi}{\partial x} d^2x}{\int I d^2x}, \quad (4.2)$$

an intensity-weighted subaperture-averaged phase gradient.

Care must be exercised in choosing the numerical derivative used in evaluating Expression (4.1). In particular, finite-difference differentiation is inappropriate because it gives large errors when the complex field varies rapidly because its phase varies with large amplitude but low spatial frequency. A Fourier derivative algorithm gives satisfactory results.

## IV.B Multidither algorithm

In the course of developing the Hartmann algorithm, we unexpectedly discovered a powerful field-based algorithm for simulating multidither correction,<sup>5</sup> an alternative to conventional adaptive optics that dispenses with wavefront sensing, and that in principle can produce an optimal Strehl ratio. This technology is currently outside the mainstream of adaptive optics research because of practical (bandwidth) limitations. In an effort to determine if such hardware limitations might be worth overcoming, the multidither algorithm was implemented in MOLLY in order to explore multidither's absolute limits. We describe the algorithm here on account of its novelty.

Multidither correction (Figure 4.1) is accomplished by a deformable-mirror-in-path optical train in which the wavefront sensor is replaced by the following hardware: a second ("dither") deformable mirror, all actuators vibrating about zero stroke with small amplitudes and distinguishable frequencies; followed by a lens (possibly including a pupil plane intensity mask); followed by an intensity detector at focal boresight. The Fourier components of the detector output at the dither frequencies are fed back to the principal deformable mirror by a hill-climbing servo that optimizes focal boresight intensity. For suitable intensity mask, and for equal beacon and outgoing wavelengths, optical reciprocity guarantees that beacon focal boresight intensity is directly proportional to outgoing far-field boresight intensity. Thus, the hill-climbing servo can simultaneously optimize boresight Strehl ratio.

Multidither modeling is challenging because literally simulating its focusing optics can place heavy demands on numerical resolution, and because literally simulating the serial processing of real multidither detector output is poorly matched to the vector architecture of a modern supercomputer. For these reasons, we have developed a multidither algorithm that refers only to pupil plane data, and that avoids explicit reference to temporal dithering.

Our multidither algorithm generates input to a hill-climbing servo by directly evaluating the derivatives of beacon focal boresight irradiance with respect to deformable-mirror actuator voltages, according to

$$\frac{\partial}{\partial v_n} (Focal Irradiance) \propto -\text{Im}\left\{\left(\int M(\mathbf{x})\psi^*(\mathbf{x})e^{-i\phi(\mathbf{x})}d^2x\right)\left(\int M(\mathbf{x})\psi(\mathbf{x})e^{i\phi(\mathbf{x})}f(\mathbf{x}-\mathbf{n}d)d^2x\right)\right\}, \quad (4.3)$$

where  $\psi$  is again beacon complex field,  $\phi$  is deformable mirror figure,  $M$  is an intensity mask,  $v_n$  is an actuator voltage,  $f$  is influence function, and the integrals are taken over the entire pupil plane of the system lens. In the limit of infinite bandwidth, the quantities (4.3) are rigorously proportional to the temporal Fourier coefficients of focal detector output at the dither frequencies. Strehl is optimal when  $M$  is proportional to the square root of outgoing irradiance.

## IV.C Phase-based algorithms

Before our field-based Hartmann model was implemented, we developed the following techniques for enhancing the realism of phase-based simulation:

Here is an algorithm for incorporating an in-path control system in a phase-based model, in the limit of infinite system bandwidth: Step 1: Set deformable mirror voltages equal (up to calibration) to wavefront-sensor phase measurements. Step 2: Construct deformable mirror figure according to Equation (2.1). Step 3: Correct the figure by Fourier transforming, multiplying the transform by

$$\frac{1}{\sum_n A(d\mathbf{p}_n)F(d\mathbf{p}_n)}, \quad (4.4)$$

where notation is the same as in Section III, and finally inverse transforming. As mentioned in Section III, the sum in expression (4.4) can be evaluated in closed form in many cases of interest.

The figure correction described above can be derived by using Fourier transforms to formally solve the linear system that determines deformable mirror actuator voltages at null wavefront-sensor output. This formal solution is not available in field-based models, for which the linear system's coefficients depend on beacon irradiance in a complicated way. In field-based models, in-path control can only be accommodated by explicitly manipulating error signals.

The sum in Equation (2.1) can be difficult to program when the influence function  $f(x,y)$  is not zero for  $|x|$  or  $|y|$  greater than one or two actuator spacings. For this reason we developed the following easily programmed algorithm for implementing long-range influence: Step 1: Choose a "reference" influence function  $f_r(x,y)$  that vanishes for  $|x|$  or  $|y|$  greater than one actuator spacing, and whose Fourier transform  $d^2F_r(dp)$  is nowhere zero. This can be done by first arbitrarily choosing two symmetric functions  $f_1(x,y)$  and  $f_2(x,y)$  that both vanish for  $|x|$  or  $|y|$  greater than one actuator spacing and that have no common zeroes in the Fourier plane, and then forming

$$f_r(\mathbf{x}) = f_1 * f_1(2\mathbf{x}) + f_2 * f_2(2\mathbf{x}), \quad (4.5)$$

where "\*" denotes convolution. Step 2: Construct deformable mirror figure according to Equation (2.1), using  $f_r$  instead of  $f$ . Step 3: Correct the figure by Fourier transforming, multiplying the transform by

$$\frac{F(dp)}{F_r(dp)}, \quad (4.6)$$

and finally inverse transforming. Of course, this algorithm is useful only when  $f_r$  and the Fourier transforms  $F$  and  $F_r$  are all known in closed form.

In principle, one can use this algorithm in field-based models, but in practice we prefer not to do so, at least when using the Hartmann model, in order to avoid unwanted interactions between Gibbs oscillations arising from the filter represented by expression (4.6) and Gibbs oscillations arising from the Fourier derivative used in the Hartmann algorithm.

## V. SIMULATIONS

We use output from MOLLY to illustrate comparison between simulation and experiment, as well as to illustrate PCI universality, in-path and out-of-path simulation, and multidither simulation.

In the course of this discussion, we shall refer to distortion number,  $N_D$ , defined by

$$N_D \equiv \int_0^\infty \left( \frac{4\sqrt{2}kP}{\rho c_p D} \right) \left( \frac{dn}{dT} \right) \left( \frac{\alpha(z)}{v(z)} \right) \exp \left\{ - \int_0^z [\alpha(z') + \alpha_s(z')] dz' \right\} dz, \quad (5.1)$$

where  $z$  is propagation distance,  $k$  is optical wavenumber,  $P$  is average outgoing power,  $D$  is beam diameter,  $\rho$  is atmospheric density,  $c_p$  is atmospheric specific heat,  $n$  is refractivity,  $T$  is temperature,  $v$  is windspeed (transverse to propagation direction),  $\alpha$  is absorption coefficient and  $\alpha_s$  is scattering coefficient. Distortion number is a rough measure of the strength of thermal blooming. In particular,  $N_D/3$  is a rough approximation to the total peak-to-valley phase distortion (in radians) due to laser-induced atmospheric heating.

*Comparison with experiment; PCI universality:* M.I.T. Lincoln Laboratory has, since 1986, been conducting an experimental laboratory study of adaptively corrected thermal blooming at high distortion number. The first phase, completed in early 1989, employed a deformable mirror with eight actuator spacings in a diameter, and provided the first experimental observation and characterization of phase-compensation instability.<sup>6</sup> The second phase, now in progress, employs a deformable mirror with sixteen actuator spacings in a diameter and greater actuator stroke, so that stronger PCI and larger distortion numbers are accessible.

A laboratory schematic is shown in Figure 5.1. The absorbing medium is  $\text{CCl}_4$ , doped with iodine. Laser wavelengths are  $0.514 \mu$  for the outgoing beam and  $0.633 \mu$  for the beacon. The outgoing beam diameter is 1 cm. Deformable mirror is in-path.

For comparison with MOLLY, we have chosen results<sup>7</sup> from an experiment with a sinusoidal intensity mask placed in front of the outgoing laser, in order to "seed" phase compensation instability. The system had one absorption cell, with thickness 11.25 cm, uniform wind oriented along an axis of the actuator grid, and actuator spacing 1.25 mm. Distortion number was 125. The sinusoidal intensity perturbation had modulation amplitude 8.75%, period twice the actuator spacing, and stripes oriented along the wind and a minimum along a midline (Figure 5.2). Results from the laboratory and from three numerical simulations are shown in Figure 5.3. The graphs in Figure 5.3 show

$$2\phi(n, m_0 + 1) - \phi(n, m_0) - \phi(n, m_0 + 2) \quad (5.2)$$

vs.  $n$ , where  $n$  is actuator number along the wind direction,  $m_0$  is the cross-wind actuator number of the midline lying along the wind,  $\phi$  is deformable mirror stroke in radians of outgoing phase, and where the data is taken after sufficient time for wind to clear the transmitting aperture. Expression (5.2) is a measure of system response to the applied perturbation. One of the three simulations is field based, with a Hartmann sensor and in-path control. The other two simulations use the phase-based model described in Section II; one phase-based simulation incorporates in-path control, the other has deformable mirror out-of-path. Figure 5.3 is noteworthy because it represents a success both for the propagation code and for the notion of PCI universality in in-path simulation: Both in-path simulations are in excellent agreement with the laboratory, while the out-of-path simulation shows weaker response to the perturbation. The two in-path simulations would differ more noticeably under more stressing conditions.

*Deformable mirror in-path vs. out-of-path:* Figure 5.4 shows peak-irradiance Strehl ratio vs. time for two field-based Hartmann simulations of outdoor propagation. In one case deformable mirror is in-path and the servo seeks-null; in the other case deformable mirror is out-of-path and actuator voltages are proportional to wavefront sensor phase measurements. In both cases, the transmitting aperture has diameter 3.5 m (obscuration 65 cm), actuator spacing is 7 cm, and wavelengths are 1.06  $\mu$  outgoing and 0.755  $\mu$  incoming. The atmospheric wind has a realistic spiral-like dependence on altitude (Figure 5.5). Thermal blooming distortion number is 185. The Fried parameter  $r_0$  of optical turbulence is roughly 12 cm. Figure 5.4 is noteworthy because it shows out-of-path performance exceeding in-path performance as foreshadowed by Figure 3.2, which showed out-of-path PCI weaker than in-path PCI.

*Phase-conjugate vs. multidither:* Figure 5.6 shows peak-irradiance Strehl ratio vs. time for Hartmann/in-path and multidither simulations of propagation with the same aperture, actuator spacing and outgoing wavelength, and through the same atmosphere as in Figure 5.3, but with incoming wavelength 1.06  $\mu$ , no turbulence and (to compensate) twice the power. Turbulence is omitted because our current implementation of the multidither algorithm requires that the aberrations to be corrected build up gradually in time from zero. Boresight Strehl ratio in the multidither simulation is equal to peak-irradiance Strehl; boresight Strehl ratio in the Hartmann simulation is less than peak-irradiance Strehl because of imperfect tilt correction. Thus, Figure 5.6 is noteworthy because the higher – although not dramatically so – peak-irradiance Strehl in the multidither case is consistent with the optimal nature of the multidither principle.

## VI. SUMMARY

We have discussed theoretical analysis and computational modeling of compensated laser propagation, especially through thermal blooming, with realistic treatment of adaptive optics hardware. Specific hardware features discussed include wavefront sensor, deformable-mirror influence function, control system, and multidither correction. Computer simulations are consistent with analysis. Simulations also agree well with a laboratory study of the onset of phase-compensation instability.

## VII. REFERENCES

1. R. R. Parenti, "Recent Advances in Adaptive Optics Methods and Technology," SPIE Vol. 1000, Laser Wavefront Control, 101-109 (1988).
2. T. J. Karr, "Thermal Blooming Compensation Instabilities," J. Opt. Soc. Am. **A6** 1038-1048 (1989).
3. J. F. Schonfeld, paper in preparation.
4. J. A. Fleck, Jr., J. R. Morris, and M. D. Feit, "Time-Dependent Propagation of High-Energy Laser Beams Through the Atmosphere," Appl. Phys. **10** 129-160 (1976).
5. T. R. O'Meara, "The Multidither Principle in Adaptive Optics," J. Opt. Soc. Am. **67** 306-315 (1977).
6. B. Johnson and C. A. Primmerman, "Experimental Observation of Phase-Conjugate Instability for Thermal-Blooming Compensation," Opt. Lett. **14** 639-651 (1989).
7. B. Johnson, Lincoln Laboratory, private communication.

This work is sponsored by the U.S. Army Strategic Defense Command, through the Department of the Air Force.

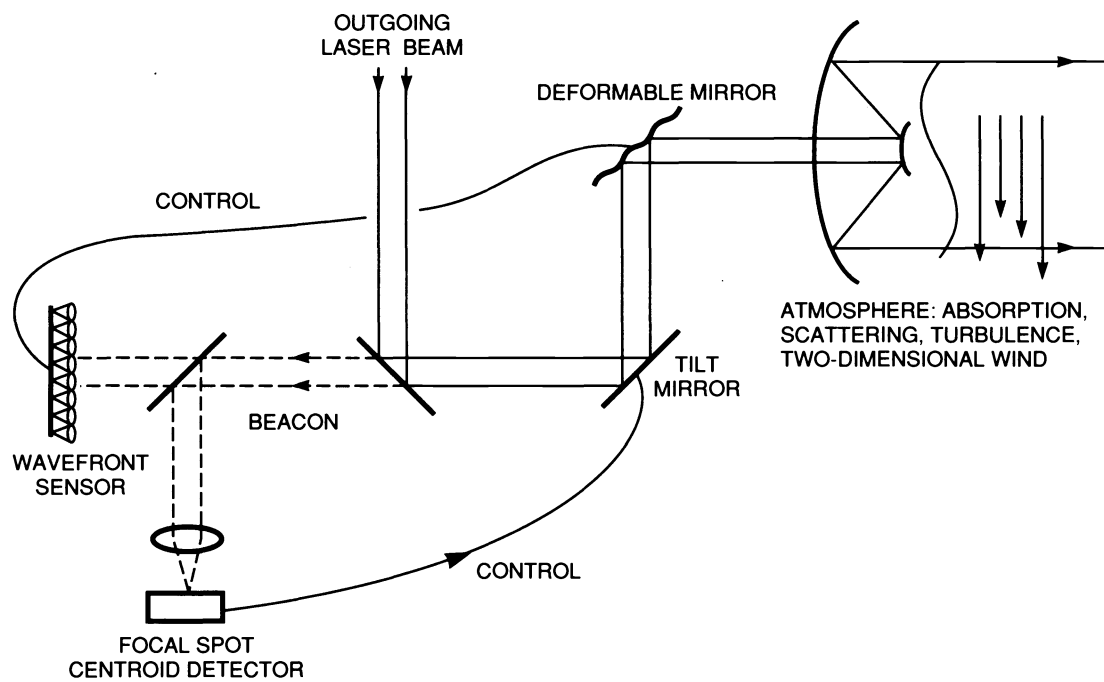


Fig. 2.1. Basic components of a conventional adaptive optics system.

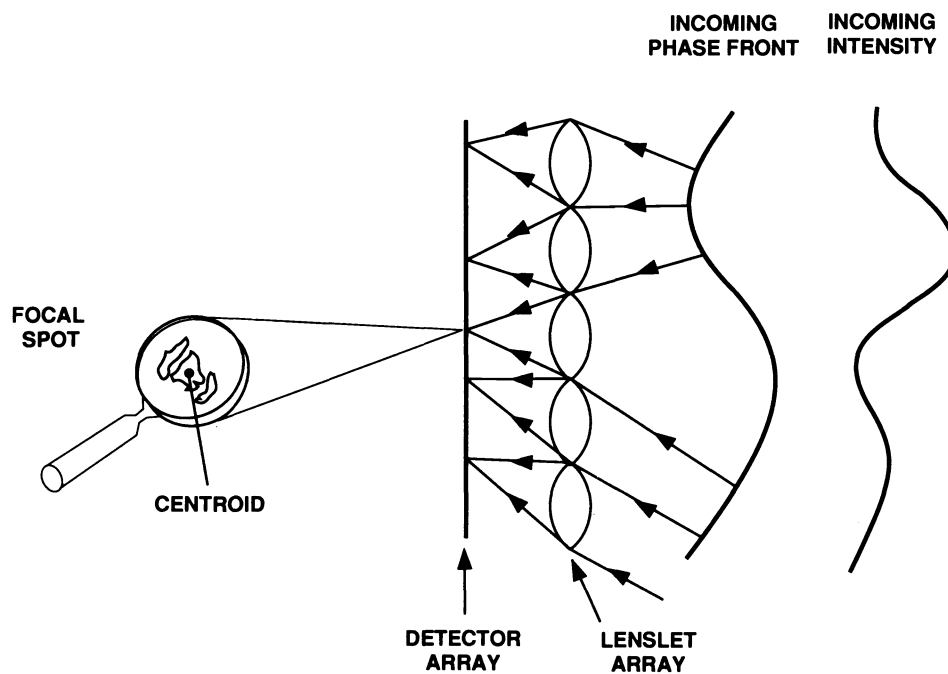


Fig. 2.2. Hartmann sensor.



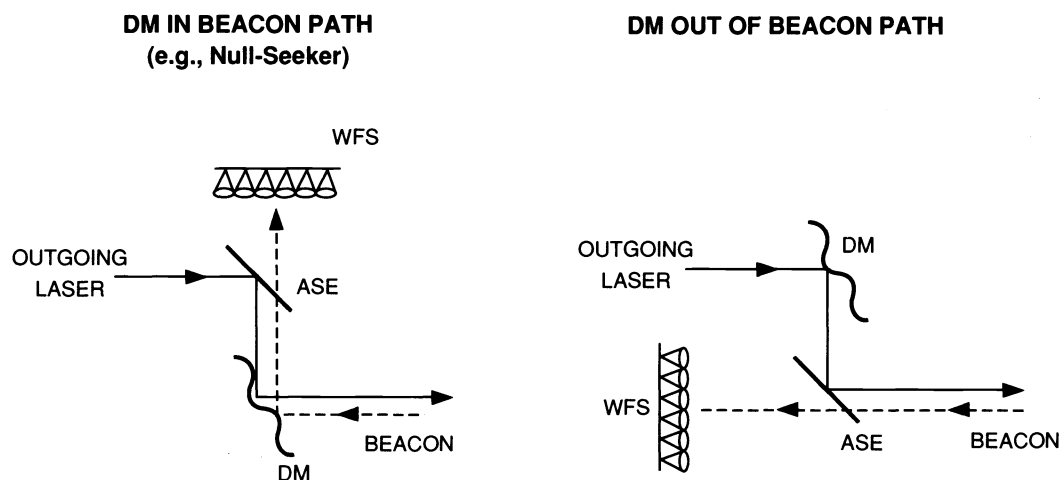


Fig. 2.3. Types of adaptive optics control. "ASE" refers to aperture-sharing element.

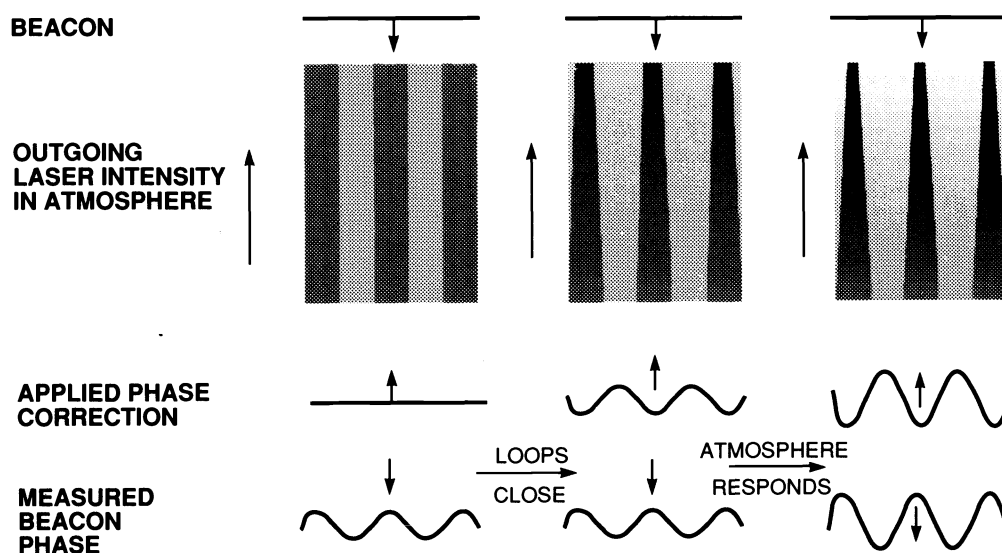


Fig. 3.1. Phase-compensation instability arises because the correction system focuses the outgoing laser beam into atmospheric hot spots, making them hotter.

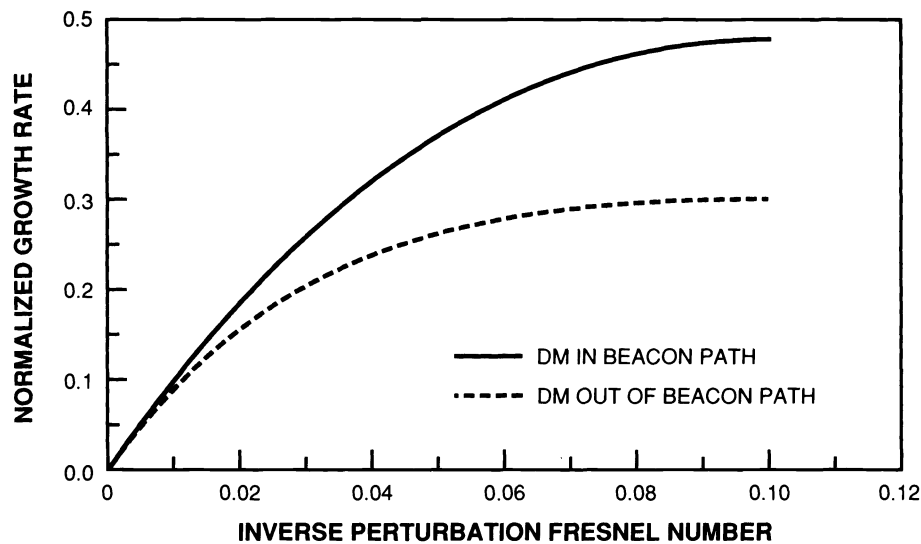
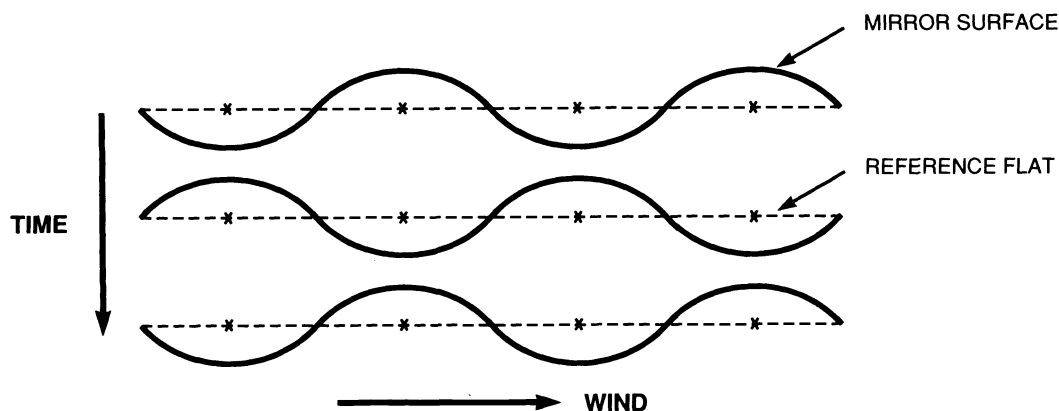


Fig. 3.2. PCI growth rates for two control laws, in an atmosphere with thermal blooming restricted to a thin slab, with Hartmann wavefront sensor and equal outgoing and incoming wavelengths. "Inverse perturbation Fresnel number" refers to  $\lambda L / \pi^3$ , where  $\lambda$  is laser wavelength,  $L$  is distance to the slab, and  $\Lambda$  is perturbation wavelength. Perturbation wavevector is at  $45^\circ$  to axes of actuator lattice. Deformable-mirror Nyquist spatial frequency corresponds to inverse perturbation Fresnel number 0.05. Slab absorptivity is hidden in growth rate normalization. Influence function is  $[1-3|x|^2+2|x|^3][1-3|y|^2+2|y|^3]$ , for  $x$  and  $y$  less than one and zero otherwise, for  $x$  and  $y$  measured in actuator spacings. Wind is ignored.

- **A NYQUIST DISTURBANCE ON A DEFORMABLE MIRROR MUST EVOLVE IN TIME AS A STANDING WAVE**



- **THE STANDING WAVE IS A SUPERPOSITION OF TWO TRAVELING WAVES, AND ONLY ONE CAN TRAVEL ALONG THE WIND AND PROMOTE POSITIVE FEEDBACK BETWEEN ADAPTIVE OPTICS AND ATMOSPHERIC HEATING**

Fig. 3.3. Intuitive explanation for the tendency of wind to halve the effective coupling for phase-compensation instability at the Nyquist spatial frequency of the deformable mirror.



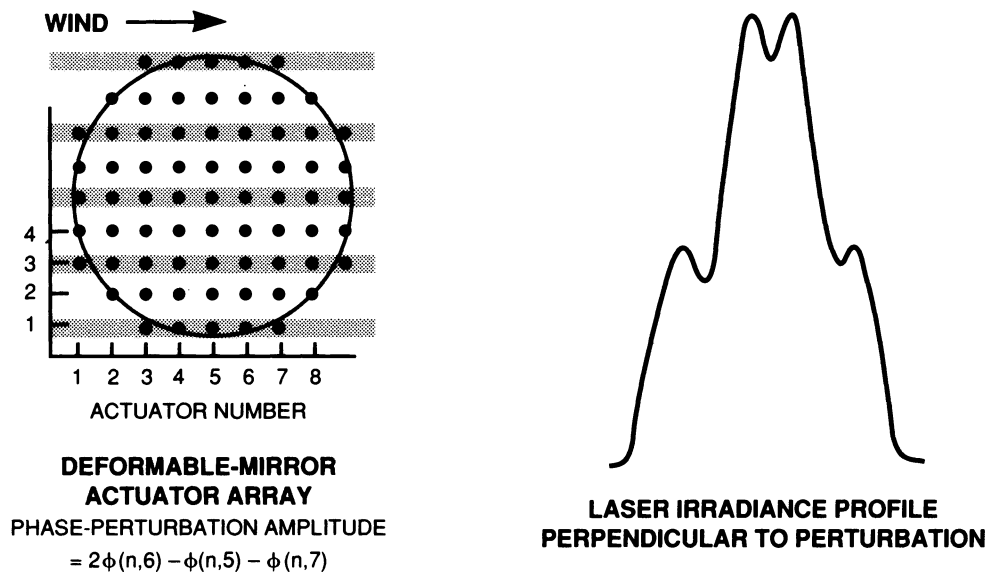


Fig. 5.2. Intensity mask for seeding phase-compensation instability (left), and perturbed outgoing irradiance (right).

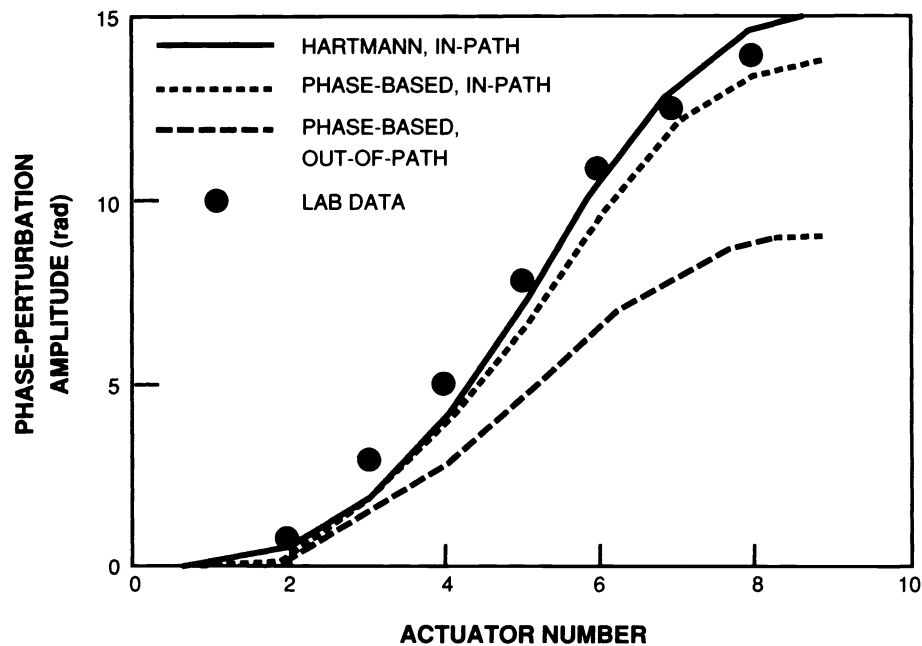


Fig. 5.3. Response of deformable mirror to intensity perturbation, according to laboratory measurements and to three simulations.

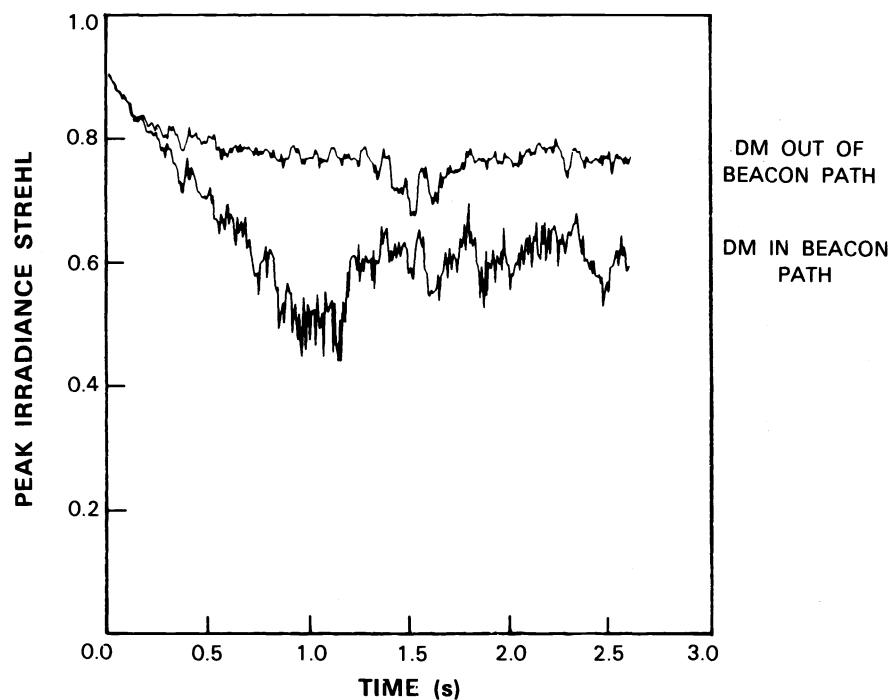


Fig. 5.4. Strehl ratio vs. time from simulations of two control laws. Total duration is twice time for slowest wind in atmosphere to clear transmitting aperture.

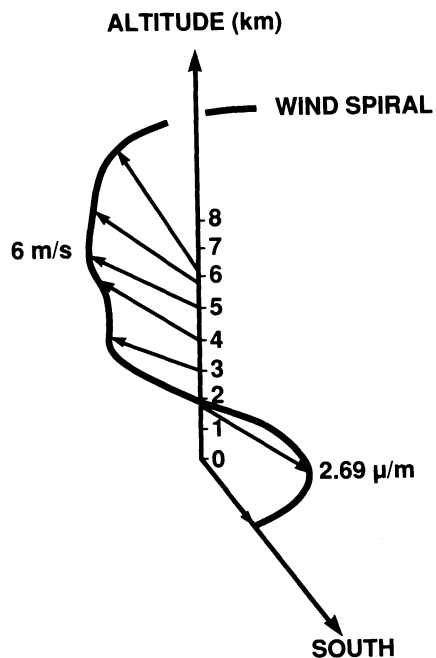


Fig. 5.5. Wind vs. altitude, as assumed in Figures 5.4 and 5.6.

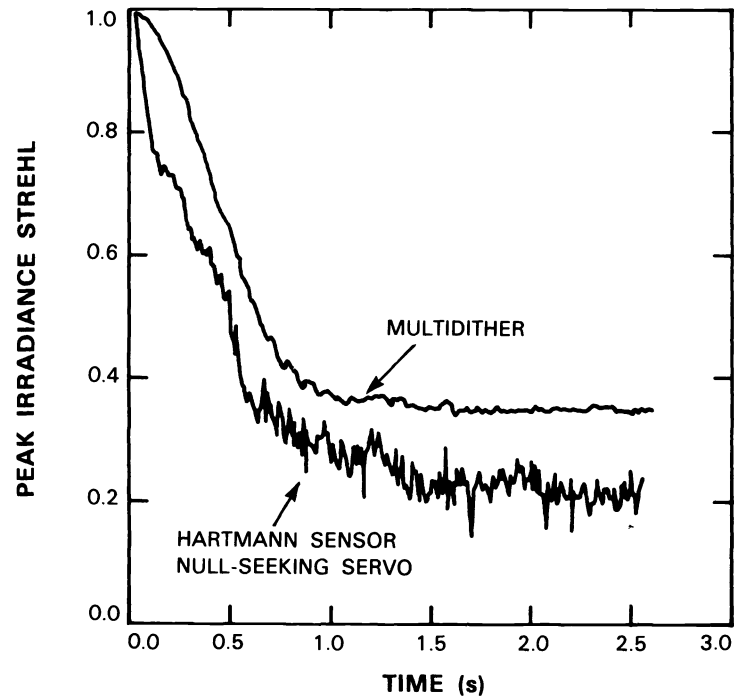


Fig. 5.6. Strehl ratio vs. time from simulations of conventional and multidither adaptive optics.